# Research on Fine Water Body Extraction From SAR Images Based on Superpixel Segmentation

Fengcheng Guo , Xiaoxiao Ma , Ning Sun , Lianpeng Zhang , and Wensong Liu

Abstract—The water body extraction technology based on superpixel segmentation in SAR images faces challenges such as insufficient precision in extracting fine water boundaries under speckle noise and complex scattering conditions. To address these issues, this article proposes an enhanced fine water body extraction method based on superpixel segmentation for SAR images. In the superpixel segmentation phase, a simple linear iterative clustering (SLIC) superpixel segmentation algorithm based on eight-direction convolution (referred to as EDC-SLIC algorithm) is introduced. This algorithm constructs three pseudo-channels using eight-direction convolution to replace the three color channels of traditional color images and employs logarithmic difference measurement in the color distance calculation part of the SLIC algorithm, thereby adapting it to the segmentation requirements of SAR images. In the water body information extraction phase, a multifeature weighted Otsu water body information extraction algorithm integrating superpixels (referred to as MFW-Otsu algorithm) is proposed. This algorithm integrates local mean and variance into a new feature image through weighting, enabling more accurate representation of texture changes in the image and enhancing the algorithm's ability to process complex image structures. The experimental results demonstrate that the EDC-SLIC algorithm and MFW-Otsu algorithm exhibit significant advantages in accuracy, robustness, and practicality. Furthermore, the integration of superpixels effectively improves the algorithm's adaptability to complex scenes, enhances detail processing capabilities, reduces misclassification phenomena, and improves the accuracy of water body information extraction.

Index Terms—Otsu, simple linear iterative clustering (SLIC), superpixel segmentation, synthetic aperture radar (SAR), water body extraction.

## I. INTRODUCTION

ATER is a fundamental natural resource essential for the survival and development of human societies and ecosystems. Rapid and accurate acquisition of water-body information and its spatial distribution is critical for national

Received 21 May 2025; revised 28 July 2025 and 6 September 2025; accepted 24 September 2025. Date of publication 30 September 2025; date of current version 17 October 2025. This work was supported by the Postgraduate Research & Practice Innovation Program of Jiangsu Province under Grant SJCX23\_1381, in part by the National Natural Science Foundation of China under Grant 62101219 and Grant 62201232, in part by the Jiangsu Provincial Natural Science Foundation of China under Grant BK20210921 and Grant BK20201026, in part by the 343 Industrial Development Project for University in Xuzhou under Grant gx2023010, and in part by the Social Welfare Project in Xuzhou City under Grant KC23304. (Corresponding author: Xiaoxiao Ma.)

The authors are with the School of Geography, Geomatic and Planning, Jiangsu Normal University, Xuzhou 221116, China (e-mail: fchguo@jsnu.edu.cn; 2020221579@jsnu.edu.cn; 2020221586@jsnu.edu.cn; zhanglp2000@126.com; liuwensongupc@163.com).

Digital Object Identifier 10.1109/JSTARS.2025.3615837

resource management, urban planning, and disaster assessment [1]. Synthetic aperture radar (SAR), an active remote-sensing technology, offers all-weather, day-and-night imaging capabilities that facilitate the detection of water bodies in shallow and shadowed regions; however, the inherent speckle noise and complex terrain-induced scattering in SAR imagery pose significant challenges to precise and detailed water body extraction.

Early work on SAR based water body extraction employed traditional image processing techniques such as grayscale histogram thresholding, region growing algorithms, and edge detection [2], [3], [4], [5], [6], [7], [8]. These methods established the foundation for SAR derived water identification but struggled with complex terrain, multiscattering effects, shadow discrimination, and sensitivity to speckle noise. With the rise of machine learning and advanced image processing methods, statistical models and support vector machines [9], [10], [11], [12], [13] as well as convolutional neural networks [14], [15], [16], [17], [18], [19] have been applied for automated water body classification. Recent years have witnessed considerable advances in superpixel segmentation for SAR imagery, driven by the development of advanced algorithms (such as SOTA) [20], [21], [22], [23], [24]. These methods have substantially enhanced the homogeneity and boundary adherence of superpixels in challenging polarimetric and complex SAR environments. Although these approaches improve detection accuracy, they remain hampered by substantial computational requirements and a heavy dependence on extensive labeled training datasets.

As the resolution of remote sensing images increases, traditional pixel-level processing methods struggle to meet precision requirements for fine water extraction in most complex scenes, though they remain effective for some simple or special scenes. Consequently, superpixel based approaches have attracted significant interest. Superpixel segmentation reduces data volume while preserving spatial structural information, thereby providing effective support for subsequent image classification and target extraction. Research into superpixel based fine water extraction methods for SAR images not only enhances extraction accuracy and robustness but also enables applications in dynamic water monitoring, environmental protection, and disaster mitigation.

Chen et al. [25] proposed a deep learning framework that integrates superpixel segmentation to extract urban water bodies from high-resolution remote sensing images. This framework isolates water features in complex urban scenes and achieves an overall accuracy (OA) of 99.14%. Pappas et al. [26] developed a river extraction pipeline for SAR imagery based on superpixel

segmentation and postclassification, enabling automated identification and planar modeling of river networks. Xiaopeng et al. [27] introduced a multisource data fusion model (MDFM) and a superpixel water extraction model (SWEM) for all weather water-body detection at the superpixel scale, which improves spatiotemporal resolution. Haoming et al. [28] presented a surface water extraction method that combines superpixels with a graph convolutional network; their results demonstrate high accuracy and strong boundary adherence even with limited training samples. Zhao et al. [29] proposed the superpixel based Detransformer (SPT) architecture, which leverages adaptive superpixel features and adjacency matrix knowledge constraints. Their SPT UNet achieves performance competitive with other state-of-the-art extraction models in both quantitative metrics and visual delineation. Li et al. [30] proposed a multiscale adaptive superpixel generation method for PolSAR images based on simple linear iterative clustering (SLIC). The results demonstrate that the proposed method provides richer multiscale detail information and significantly improves segmentation outcomes.

However, these methods are tailored to specific scenarios and do not generalize well to SAR-based water body extraction. Moreover, many of them incur long computation times and high resource demands, especially for high-resolution images or multi-iteration workflows. In contrast, the proposed method, building upon superpixel segmentation and enhanced traditional algorithms, offers a computationally efficient alternative that requires minimal training data. This approach specifically addresses SAR challenges such as speckle noise and complex scattering by introducing novel adaptations:

- 1) constructing pseudo-channels via eight-direction convolution to enrich single-channel SAR data representation;
- 2) incorporating logarithmic difference and edge weighting in the superpixel distance metric for improved robustness to intensity variations and boundary adherence; and
- integrating local mean and variance features into a weighted Otsu thresholding framework to enhance texture awareness and noise suppression.

These modifications aim to bridge the gap between traditional pixel-level methods and the representational power needed for fine water body extraction in complex SAR scenes, without the heavy resource demands of deep learning models.

# II. FUNDAMENTALS OF SUPERPIXEL SEGMENTATION AND WATER INFORMATION EXTRACTION

The SLIC algorithm offers several benefits, including a low number of iterations, compact superpixel shapes, and high boundary adherence. Consequently, we introduce the EDC-SLIC superpixel segmentation algorithm, which is tailored for SAR imagery. First, three pseudo-channels are generated via eight-direction convolution to emulate the three color channels of optical images. Then, the color-distance computation within the original SLIC framework is optimized to better accommodate the scattering characteristics of SAR data. In water-body extraction, the Otsu thresholding method is favored for its automation, statistical optimality, and computational efficiency. To address the complex speckle noise and heterogeneous texture

of SAR images, we propose an MFW-Otsu algorithm. This approach incorporates additional feature weights into the thresholding process, thereby improving robustness and accuracy in challenging SAR scenarios.

#### A. SLIC Superpixel Segmentation Algorithm

The SLIC algorithm adapts the K-means clustering paradigm [31] to partition an image into uniform and structurally coherent superpixel regions. A superpixel is defined as a spatially connected group of pixels sharing similar attributes, such as intensity and texture. By jointly optimizing feature distances in both color (or intensity) and spatial domains, SLIC delivers accurate segmentation results with high computational efficiency.

The SLIC algorithm begins by determining the target superpixel size from the user-specified number of superpixels and then places clustering centers on a regular hexagonal grid across the image. A hexagonal grid achieves a more uniform spatial covering than a square grid. Each cluster center marks the initial centroid of a superpixel, with all superpixels initially having approximately equal size. This initialization ensures that subsequent clustering proceeds from a spatially balanced configuration and preserves superpixel uniformity [32]. The expected superpixel size S is given by

$$S = \sqrt{N/k}. (1)$$

Here, N is the total number of pixels in the image, k is the desired number of superpixels, and S represents the average area of each superpixel (i.e., the side length of each superpixel).

Second, SLIC employs a composite distance metric to quantify the similarity between each pixel and a given cluster center. This metric balances color similarity against spatial proximity, producing superpixels that are both spectrally homogeneous and spatially compact. The formula for comprehensive distance measurement D is

$$D(P_i, C_k) = \sqrt{(d_c^2 + ((d_s^2)/S)^2 \cdot m^2)}.$$
 (2)

Here, the color distance dc refers to the color distance, indicating the difference between pixels  $P_i$  and cluster centers  $C_k$  in the Lab color space

$$d_c = \sqrt{(L_i - L_k)^2 + (a_i - a_k)^2 + (b_i - b_k)^2}.$$
 (3)

In (2), ds is the spatial distance, representing the distance between the pixel  $P_i$  and the cluster center  $C_k$  in the image coordinates:

$$d_s = \sqrt{(x_i - x_k)^2 + (y_i - y_k)^2}. (4)$$

Here,  $D(P_i, C_k)$  denotes the composite distance between the pixel  $P_i$  and the cluster center  $C_k$ . S is the expected superpixel size (the square root of the average superpixel area), which normalizes the spatial distance. The parameter m balances color similarity against spatial compactness and typically ranges from 10 to 40. Higher values of m encourage more regular, compact superpixel shapes, whereas lower values place greater emphasis on preserving color homogeneity.

Unlike standard K-means algorithm, SLIC algorithm confines pixel assignment to a local neighborhood around each cluster center. For each cluster center  $C_k$ , only pixels within a  $2S \times 2S$  window are considered, rather than evaluating the entire image. Within this window, the composite distance  $D(P_i, C_k)$  is computed for each pixel  $P_i$ . If a pixel's distance to center  $C_k$  is smaller than its current assignment, its label is updated to  $C_k$ . After all pixels have been evaluated, each cluster center is repositioned by averaging the Lab color coordinates and spatial coordinates of the pixels assigned to it

$$C_k = (1/N_k) \sum_{i=1}^{N_k} P_i.$$
 (5)

Here,  $N_k$  denotes the number of pixels assigned to the kth cluster, and  $P_i$  is the color and position vector of these pixels. The algorithm iteratively updates both the cluster centroids and pixel labels, thereby refining the superpixel segmentation with each iteration.

After clustering converges, SLIC applies morphological operations to enforce connectivity of the superpixel regions. In practice, image noise or complex structures can produce small, isolated pixel groups. To eliminate these artifacts, SLIC merges any disconnected pixel clusters into neighboring superpixels, ensuring that each superpixel forms a single connected component. This post-processing step suppresses spurious segments and further smooths superpixel boundaries, thereby enhancing the spatial coherence of the segmentation results.

#### B. Otsu Thresholding Method

The Otsu algorithm [33] is a widely used adaptive thresholding method for image segmentation, especially effective in the binarization of grayscale images. Its primary objective is to automatically determine an optimal threshold based on the image's grayscale histogram, thereby separating the image into two classes: foreground and background. This method is particularly suitable for images with a bimodal grayscale distribution, where the foreground and background exhibit distinct intensity differences. The core principle of the Otsu algorithm is to exhaustively search for the threshold that maximizes the between-class variance (or equivalently, minimizes the within-class variance). In this way, it ensures the best possible separation between the two classes. This approach is also known as the maximum between-class variance method. One of the key strengths of the Otsu algorithm is its automation. It requires no manual intervention or prior knowledge about the image content, making it highly adaptable to various imaging scenarios.

For a grayscale image, the grayscale value of pixels is usually between 0 and 255. Suppose the gray value range of the image is [0, L-1], where L is the gray level (usually 256). The Otsu algorithm first calculates the gray histogram of the image, that is, counts the number of pixels for each gray value, denoted as h(i), where i is the gray value, h(i) represents the number of pixels corresponding to that gray value. Based on the histogram, calculate the probability distribution of each gray value:

$$p(i) = h(i)/N. (6)$$

Here, N represents the total number of pixels in the image, p(i) indicates the proportion of pixels with a gray value i of in the image.

Then, the Otsu algorithm divides the image into two categories, the target and the background, by traversing all possible gray thresholds t. For each possible threshold t, the algorithm can calculate the pixel ratio (i.e., weight) of the target and the background, as well as their gray-level mean values. The weight of the target class (i.e., the proportion of the total number of pixels) can be expressed as

$$\omega_1(t) = \sum_{i=t}^{L-1} p(i). \tag{7}$$

Its gray mean value can be expressed as

$$\mu_{1}\left(t\right) = \left(\sum_{i=t}^{L-1} i \cdot p\left(i\right)\right) / \omega_{1}\left(t\right). \tag{8}$$

The weights of the background class can be expressed as

$$\omega_2(t) = \sum_{i=0}^{t-1} p(i).$$
 (9)

Its gray mean value can be expressed as

$$\mu_2(t) = \left(\sum_{i=0}^{t-1} i \cdot p(i)\right) / \omega_2(t). \tag{10}$$

The core idea of the Otsu algorithm is to determine the optimal segmentation threshold t by maximizing the interclass variance, which quantifies the separability between the target and background classes. A larger interclass variance indicates a clearer distinction between the two classes, leading to a more effective segmentation result. The formula for inter-class variance is

$$\sigma_B^2(t) = \omega_1(t) \cdot \omega_2(t) \cdot \left[\mu_1(t) - \mu_2(t)\right]^2. \tag{11}$$

The Otsu algorithm traverses each possible threshold t, calculates its corresponding interclass variance  $\sigma_B^2(t)$ , and then selects the threshold  $t^*$  that maximizes the interclass variance as the optimal segmentation threshold

$$t^* = \arg\max_{A} \sigma_B^2(t). \tag{12}$$

This threshold  $t^*$  is the one that maximizes the difference between the target and the background classes. Once the optimal threshold  $t^*$  is determined, binarization operation can be performed on the image. That is, pixels with a gray value less than  $t^*$  are marked as the background, and pixels with a gray value greater than  $t^*$  or equal to  $t^*$  are marked as the target. The binarized image can be represented as

$$B(x,y) = \begin{cases} 1, & \text{if } I(x,y) < t^* \\ 0, & \text{otherwise} \end{cases}$$
 (13)

Among them, B(x,y) is the binarized image of the output and I(x,y) is the grayscale image of the input.

## C. Postprocessing Techniques

To further enhance the accuracy of water body extraction, this paper applies several post-processing techniques to the binarized

images, including morphological operations such as opening and closing, as well as Gaussian filtering for edge smoothing. These operations are crucial for refining object boundaries and improving segmentation quality. Morphological opening is primarily used to remove small isolated noise and to disconnect narrow bridges between regions. It consists of an erosion operation followed by a dilation operation. This process helps eliminate irrelevant details without significantly affecting the shape of the main water regions. Morphological closing, on the other hand, is used to fill small holes within segmented regions and to connect fragmented parts of water bodies. It is the reverse of opening and involves a dilation operation followed by erosion. This operation enhances the continuity of segmented objects and reduces fragmentation. In addition, Gaussian filtering is employed to smooth the edges of the extracted water regions. By reducing sharp transitions and noise along the boundaries, it helps produce cleaner and more visually consistent segmentation results.

The basic principle of the erosion operation is to slide a structuring element (SE) across the image and apply a local minimum operation within the neighborhood defined by the SE. At each pixel location, the SE is overlaid on the image, and the minimum pixel value covered by the SE is assigned to the central pixel. This process effectively shrinks bright regions (typically foreground objects), removes small white noise, and thins object boundaries. In contrast, the dilation operation performs the opposite function. It uses the same sliding SE approach but applies a local maximum operation instead. For each position, the maximum pixel value within the neighborhood defined by the SE is assigned to the central pixel. Dilation expands the bright areas in the image, helping to fill small holes within objects, connect adjacent regions, and thicken object boundaries. Together, erosion and dilation serve as the building blocks for more advanced morphological operations like opening and closing, and play a critical role in noise removal and structure refinement in binary image processing.

Gaussian filtering is a widely used smoothing technique in image processing, primarily aimed at reducing noise and fine details while preserving the overall structure of the image. Unlike simple mean filtering, which assigns equal weight to all neighboring pixels, Gaussian filtering applies a weighted average based on a Gaussian distribution, giving more importance to pixels closer to the center of the filter window. The weight of each pixel in the filtering process is determined by the two-dimensional Gaussian function, defined as

$$G(x,y) = \frac{1}{2\pi\sigma^2} \exp\left(-\frac{x^2 + y^2}{2\sigma^2}\right). \tag{14}$$

Here, (x,y) is the coordinate of the pixel,  $\sigma$  is the standard deviation of the Gaussian distribution, and determines the degree of smoothness. Larger  $\sigma$  values will lead to a stronger smoothing effect.

Gaussian filtering is achieved by convolving the Gaussian kernel with the image. Specifically, Gaussian filtering first builds a Gaussian kernel of  $(2k+1)\times(2k+1)$  size based on the specified  $\sigma$  values, where k usually takes  $3\sigma$ . Then, slide the Gaussian kernel on the image. For each pixel position, calculate

the weighted sum of its neighborhood pixel value and the corresponding element of the Gaussian kernel, and assign the result to that position. Its formula is

$$I'(x,y) = \sum_{i=-k}^{k} \sum_{j=-k}^{k} I(x+i,y+j) \cdot G(i,j).$$
 (15)

Here, I(x, y) is the original image, I'(x, y) is the filtered image, and G(i, j) is the value of the Gaussian kernel at the position (i, j).

Gaussian filtering is highly effective in smoothing images and suppressing noise while preserving important structural details. Compared to simple average filtering, its main advantage lies in the use of a Gaussian-weighted kernel, which assigns greater importance to pixels closer to the center of the filter. This allows it to reduce noise without significantly blurring edges or distorting object boundaries. This characteristic is particularly valuable for tasks such as water body extraction, where maintaining edge clarity is essential for accurate delineation.

# III. PROPOSED WATER BODY INFORMATION EXTRACTION METHOD BASED ON SUPERPIXEL SEGMENTATION

This article presents a water body extraction method for SAR images based on superpixel segmentation, which is structured into five core stages: SAR image preprocessing, EDC-SLIC superpixel segmentation, water body extraction using the MFW-Otsu algorithm, postprocessing, and accuracy evaluation and analysis. Each stage is designed to build upon the previous one, ensuring a progressive and integrated workflow that culminates in the accurate extraction of water body information. The overall methodological framework is illustrated in Fig. 1.

### A. EDC-SLIC Superpixel Segmentation Algorithm

The core framework of the EDC-SLIC algorithm follows the same foundational structure as the original SLIC algorithm, as described in (1)–(5). In this approach, each image pixel is represented by a five-dimensional feature vector that integrates both color and spatial information. The algorithm then performs an iterative optimization process similar to K-means clustering within this five-dimensional feature space. During each iteration, the clustering centers are updated by minimizing the weighted sum of color and spatial distances. This strategy ensures that pixels with similar visual and positional characteristics are grouped together. As the iterations proceed, the algorithm progressively refines the segmentation, ultimately producing compact, spatially coherent, and perceptually meaningful superpixel regions.

However, in SAR images, relying solely on conventional color distance calculations is insufficient to capture the true similarity between pixels, due to the presence of speckle noise and limited spectral information. To address this limitation, this article introduces an improvement to the color distance calculation component, as defined in (3). Specifically, a logarithmic difference measure is adopted to enhance contrast and better reflect subtle variations in pixel intensity. This modification strengthens the algorithm's ability to distinguish between water bodies and complex background features in SAR imagery, leading to more

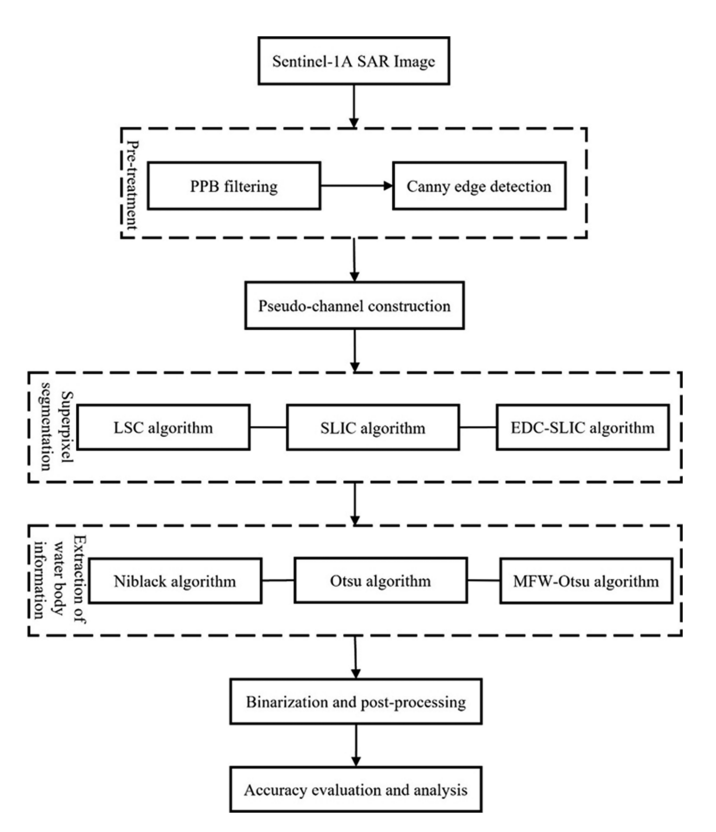


Fig. 1. Overall technical flowchart.

accurate and robust segmentation results:

$$d_c = \sum_{n=1}^{3} 30 \cdot \log \left( \frac{I_n + 1e - 10}{C_n + 1e - 10} \right) + \log \left( \frac{C_n + 1e - 10}{I_n + 1e - 10} \right)$$
(16)

where  $I_n$  represent the intensity values of pseudo-channel n, and  $C_n$  is a small constant added to prevent numerical instability when intensities are close to zero.

This logarithmic transformation enhances the robustness of color distance calculations, particularly in scenarios involving significant intensity variations, making it well-suited for processing SAR images. In addition, to more effectively capture edge information within SAR images, the algorithm incorporates edge intensity into the distance computation. Specifically, an edge intensity subgraph is introduced, derived from the results of Canny edge detection. Canny edge detection is adopted due to its effective edge localization and noise robustness, critical for preserving fine water-land boundaries in speckle-prone SAR images. This edge-aware enhancement allows the algorithm to assign greater importance to pixels located near significant boundaries

$$D = D + W_e \cdot d_e. \tag{17}$$

Here,  $W_e$  is the weight of the edge strength, which  $d_e$  is the strength value calculated through edge detection.

 $W_e$ = 10 is empirically set to balance edge adherence and region homogeneity. This value scales edge intensity to match the magnitude of color distance. It is independent of Canny thresholds, which are fixed at default values.

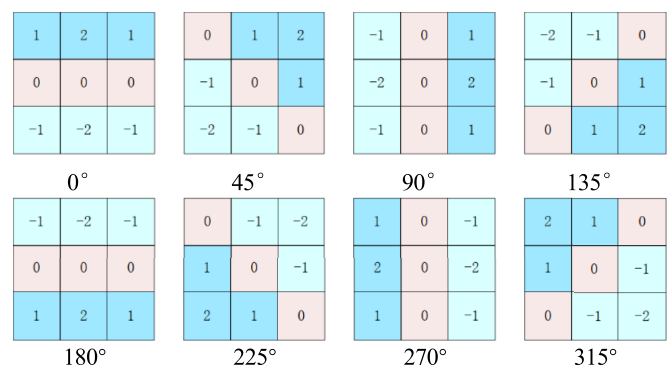


Fig. 2. Eight-direction convolutional template.

This improvement ensures that edge features are fully integrated into the distance measurement process, significantly enhancing the quality of superpixel segmentation. By emphasizing edge information, the algorithm better preserves boundary details, leading to more precise and coherent segmentation results, especially in areas with complex textures or subtle transitions. This refinement ultimately contributes to improved accuracy in subsequent water body extraction from SAR images.

#### B. Pseudo-Channel Construction

To compensate for the limited information inherent in singlechannel SAR images, this article constructs three pseudochannels based on feature extraction and processing techniques tailored to SAR data. These pseudo-channels provide richer and more discriminative feature representations, which support more effective superpixel segmentation. Specifically, these three pseudo-channels extract the key information of the image from three dimensions: local texture, statistical features and global gradient respectively. By fusing these multidimensional features, the proposed approach enhances the superpixel segmentation algorithm's adaptability to complex SAR scenes, improving its ability to distinguish between different land covers and water bodies.

Pseudo-channel 1 captures local features and edge information in the SAR image by applying convolution kernels oriented in multiple directions, as illustrated in Fig. 2. This approach is effective for detecting texture variations, particularly in complex scenes, such as the boundaries between water bodies and land, enabling clear differentiation of edge features among various ground objects. Specifically, suppose there are K convolution kernels  $K_i$ , and the construction of pseudo-channel 1 can be expressed as

$$I_1(x, y) = \max(\text{conv2}(I, K_i)), i \in \{1, 2, \dots, K\}.$$
 (18)

Here, I is the input SAR image;  $\operatorname{conv2}(I, K_i)$  indicates that the image I is a convolution operation with the convolution kernel  $K_i$ , and pseudo-channel 1 is constructed by taking the maximum response value in each direction. This step effectively enhances edge and texture features within the image, particularly in regions exhibiting significant multidirectional texture variations, such as the boundaries of water bodies. By emphasizing these

directional responses, the method improves the distinction between adjacent surfaces, facilitating more accurate segmentation in complex SAR scenes.

Pseudo-channel 2 characterizes the intensity variations of each pixel by computing statistical features—such as the mean and standard deviation—within its local neighborhood. These statistical measures effectively capture local texture changes and help mitigate the impact of speckle noise. For each pixel (x,y), the construction formula of pseudo-channel 2 is

$$I_2(x,y) = \sqrt{\sigma(x,y) \cdot \mu(x,y)}.$$
 (19)

Here,  $\sigma(x,y)$  is the standard deviation of the area where the pixel (x,y) is located, representing the volatility of the intensity of this area;  $\mu(x,y)$  is the mean value of the area where the pixel (x,y) is located, reflecting the intensity level of that area.

By combining the mean and standard deviation, pseudochannel 2 effectively captures local texture variations while balancing noise suppression and feature enhancement. This synergy allows the algorithm to maintain stable feature extraction even in regions with substantial noise interference. The statistical feature space created by this channel complements the convolutional features of pseudo-channel 1, together improving the accuracy and robustness of superpixel segmentation when addressing the complex scattering characteristics inherent in SAR images.

Pseudo-channel 3 captures the overall structural characteristics of the image by computing global gradient information, thereby increasing the algorithm's sensitivity to boundaries during segmentation. Specifically, this channel employs a multiscale gradient operator to calculate the gradient magnitude and direction at the pixel level, effectively extracting geometric and edge features present in SAR images. In complex scattering environments, these global gradient features robustly highlight boundary intensity differences between various ground object types. Consequently, this pseudo-channel is crucial for enhancing the precision of superpixel segmentation. The construction of pseudo-channel 3 can be expressed as

$$I_3(x,y) = \sqrt{G_x^2(x,y) + G_y^2(x,y)}.$$
 (20)

Here,  $G_x(x,y)$  is the gradient of the image in the horizontal direction, which is usually calculated by the Sobel operator or other edge detection operators;  $G_y(x,y)$  is the gradient of the image in the vertical direction. Global gradient information effectively enhances boundary features within the image. In particular, at the interfaces between water bodies and land, gradient values tend to be high, which significantly aids in improving segmentation accuracy by clearly delineating these transitions.

After constructing the three pseudo-channels, they are integrated into a three-channel "pseudo-color" image, which serves as the input to the EDC-SLIC algorithm for superpixel segmentation

$$I_{\text{pseudo}}(x, y) = [I_1(x, y), I_2(x, y), I_3(x, y)].$$
 (21)

By fusing multiple features in this way, the pseudo-color image simultaneously captures local texture, statistical characteristics, and global structural information. This richer feature representation enhances the input data for the EDC-SLIC algorithm, significantly improving its segmentation accuracy and robustness when applied to SAR images.

#### C. MFW-Otsu Algorithm

Traditional Otsu algorithm performance is limited when handling the complex noise and diverse texture structures present in SAR images. To address this, this study proposes the MFW-Otsu algorithm that enhances adaptability by incorporating both local mean and variance information. This approach generates a new feature image through a weighted combination of these local statistics, enabling a more accurate representation of texture variations within the image. As a result, the enhanced method not only improves handling of complex image structures but also significantly suppresses noise interference, making it especially well-suited for SAR images characterized by intricate noise and texture patterns. The local mean  $\mu$  is calculated as follows:

$$\mu(x,y) = \frac{1}{N} \sum_{i=-1}^{1} \sum_{j=-1}^{1} I(x+i,y+j).$$
 (22)

Calculation of local variance  $\sigma$ 

$$\sigma(x,y) = \sqrt{\frac{1}{N} \sum_{i=-1}^{1} \sum_{j=-1}^{1} (I(x+i,y+j) - \mu(x,y))^{2}}.$$
(23)

Next, the local mean and local variance are combined using a weighted approach to generate a new feature image. This fused feature captures both the intensity variations and the local variability, thereby enhancing the texture representation within the image. The calculation formula for the combined feature is

$$I_{\text{combined}} = \alpha \cdot \mu(x, y) + (1 - \alpha) \cdot \sigma(x, y). \tag{24}$$

Here, N is the window size (for example, a  $3 \times 3$  window); I(x,y) is the gray value of the pixel;  $\alpha$  is a weighting parameter that controls the relative importance of the mean and variance in the combined features.

To analyze the sensitivity of parameter  $\alpha$ , this study incrementally increased its value by 0.1, conducting comparative experiments across the range  $\alpha=0.1$ –1.0. The results indicate that: Lower values of  $\alpha$  (< 0.5) emphasize local variance, enhancing texture discrimination but amplifying noise. This leads to increased water fragmentation and a relatively lower OA; moderate values of  $\alpha$  (0.5–0.8) yield a relatively balanced outcome, achieving superior performance in most scenarios; higher values of  $\alpha$  (> 0.8) emphasize the local mean, effectively suppressing noise. However, this tends to blur intricate texture boundaries, consequently reducing accuracy.

Considering these factors comprehensively,  $\alpha=0.8$  was selected for this study. This value effectively suppresses noise while producing relatively robust results.

# IV. EXPERIMENTAL RESULTS AND ANALYSIS

This study utilizes SAR data from the Sentinel-1A satellite as the primary data source. Launched on 3 April 2014, Sentinel-1A operates in a near-polar sun-synchronous orbit and is part of the

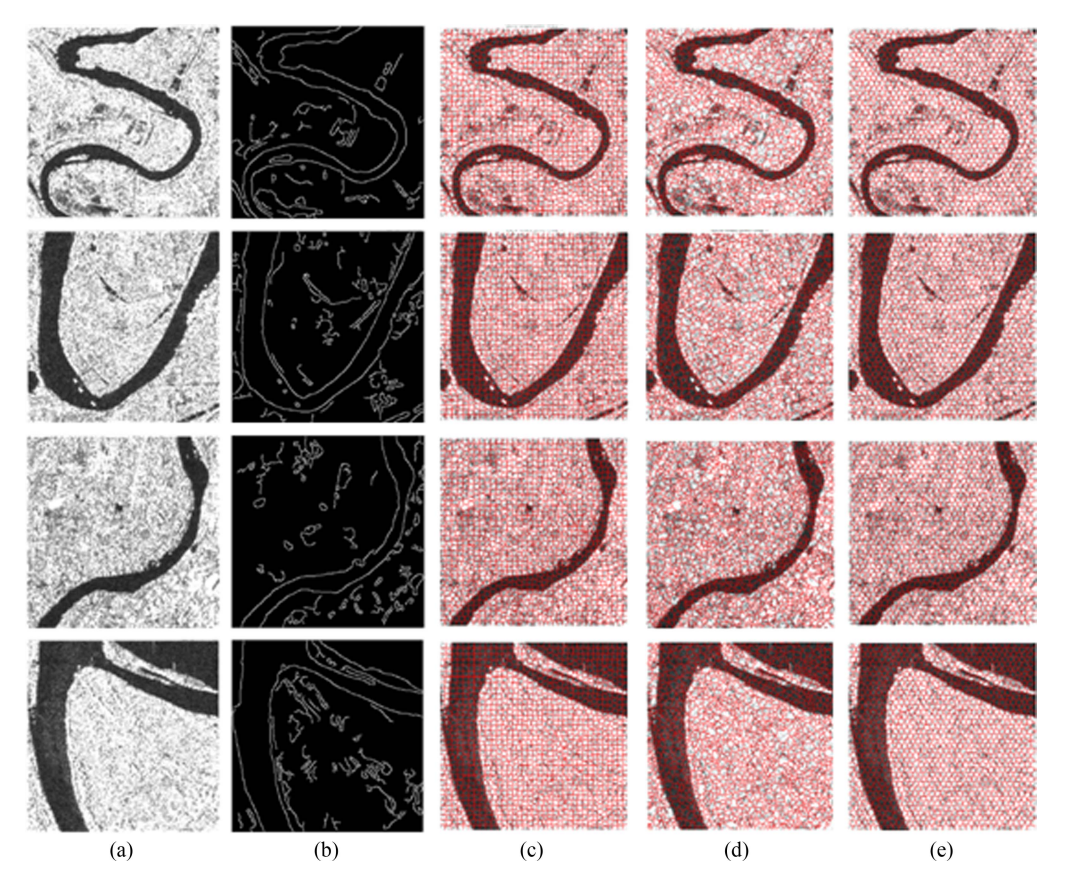


Fig. 3. Superpixel segmentation results. (a) Original image. (b) Canny edge detection result. (c) Superpixel segmentation result of the LSC algorithm. (d) Superpixel segmentation result of the SLIC algorithm.

European Space Agency's Copernicus program. The satellite is equipped with a C-band SAR and orbits at an altitude of 693 km. Its revisit period is 12 days for a single satellite and 6 days when operating in tandem with its sister satellite. Sentinel-1A supports four imaging modes; for this experiment, the ground range detected (GRD) products acquired under the interferometric wide swath mode were selected. The image data used were captured on 24 June 2024 and 19 December 2024.

Four distinct water body scenarios were selected for the experiment. Scene 1 features a water body with significant bends, forming multiple curves. Scene 2 presents a gently bending water body with a large, smooth curve and includes ships within the scene. Scene 3 contains a relatively straight water body with minimal curvature. Scene 4 exhibits a water body with a high degree of curvature accompanied by discontinuities.

# A. Superpixel Segmentation Experiment

In this study, three superpixel segmentation methods-namely the LSC algorithm, the standard SLIC algorithm, and the SLIC algorithm enhanced with eight-direction convolution-were applied to the same SAR image. The number of superpixels was set to 500, 900, and 1300, respectively, generating a total of 36 segmentation outputs across four different regional images. Experimental results indicate that the segmentation performance is optimal when the number of superpixels is set to

1300. Therefore, when conducting the research on the extraction of water body information, this paper selects the segmentation result corresponding to the 1300 superpixel setting.

Fig. 3 presents a comparison of the segmentation effects produced by the three algorithms under the same superpixel number setting. Fig. 4 shows the segmentation effects of the three algorithms under the settings of 500 and 900 superpixels. And Fig. 5 shows the detailed display of the superpixel segmentation results of the three algorithms. From the visualization results, it is evident that both the LSC algorithm and the traditional SLIC algorithm exhibit certain limitations in accurately fitting object boundaries. Specifically, in areas where the target contour exhibits significant curvature, the superpixel boundaries produced by these two methods demonstrate marked rigidity and do not closely adhere to the intricate geometric shapes of the targets. In addition, the SLIC algorithm demonstrates inferior shape retention capabilities; its superpixel boundaries appear disordered and lack coherent spatial consistency.

In contrast, the EDC-SLIC algorithm demonstrates notable advantages in superpixel segmentation performance, particularly for SAR images. By incorporating eight-direction convolution kernels, it effectively extracts multidirectional edge and texture features. Combined with an improved distance metric that considers edge intensity and logarithmic contrast, the algorithm is better suited to handle the complex characteristics and high variability in SAR imagery. Experimental results

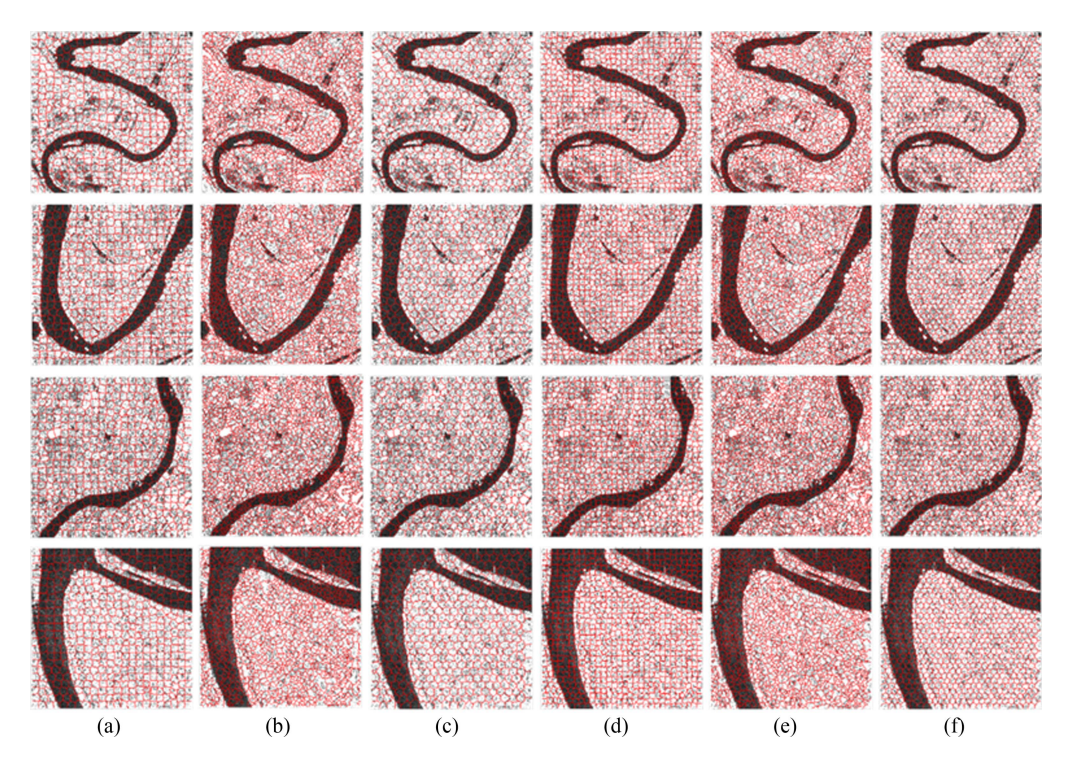


Fig. 4. Superpixel segmentation results. (a) Segmentation result of the LSC algorithm under the setting of 500 superpixels. (b) Segmentation result of the SLIC algorithm under the setting of 500 superpixels. (c) Segmentation result of the EDC-SLIC algorithm under the setting of 500 superpixels. (d) Segmentation result of the LSC algorithm under the setting of 900 superpixels. (e) Segmentation result of the SLIC algorithm under the setting of 900 superpixels. (f) Segmentation result of the EDC-SLIC algorithm under the setting of 900 superpixels.

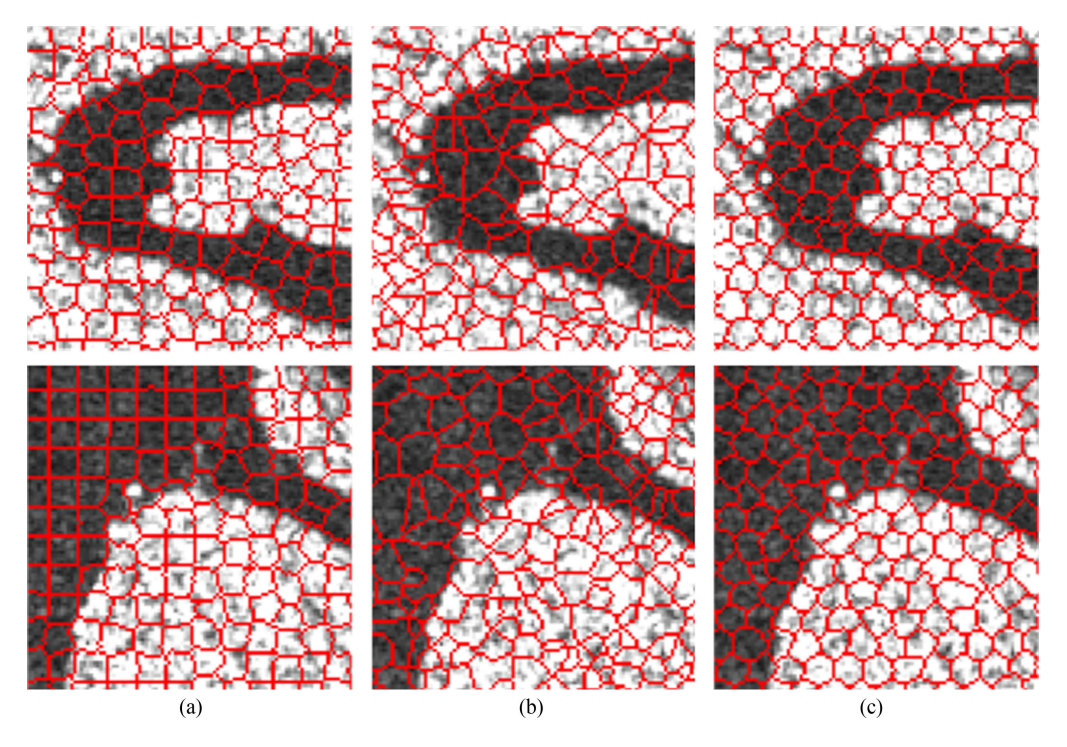


Fig. 5. Detailed image of the superpixel segmentation result. (a) Superpixel segmentation result of the LSC algorithm. (b) Superpixel segmentation result of the SLIC algorithm.

Scene	Precision parameter	LSC algorithm	SLIC algorithm	EDC-SLIC algorithm
1	BR	19.76%	15.44%	19.96%
	UE	13.71%	14.30%	14.37%
	OE	18.20%	29.16%	15.99%
	T	2.527	1.609	2.637
	BR	17.39%	17.91%	20.15%
2	UE	10.50%	10.59%	11.50%
	OE	5.81%	5.88%	3.86%
	T	4.649	4.737	6.972
3	BR	15.75%	15.29%	16.22%
	UE	15.22%	10.11%	15.77%
	OE	7.16%	14.65%	4.49%
	T	3.235	2.556	4.641
4	BR	28.17%	27.91%	28.94%
	UE	4.38%	4.34%	4.80%
	OE	5.85%	7.07%	5.73%
	T	11.247	10.379	11.080

TABLE I
PRECISION RESULTS WHEN THE NUMBER OF SUPERPIXELS IS SET TO 500

indicate that EDC-SLIC not only achieves more accurate boundary alignment with real-world targets but also excels in preserving object shapes. In regions with curved geometries, the superpixel boundaries generated by EDC-SLIC are smoother, more continuous, and follow target contours more precisely compared to those from LSC and traditional SLIC algorithms. Across all four test scenarios, the EDC-SLIC algorithm consistently maintained superior performance, accurately delineating the contours of ground objects. Even in cases involving significant background complexity or highly curved water bodies, the algorithm showed no notable degradation in performance highlighting its robustness and adaptability. Its flexibility in boundary definition and ability to accommodate complex geometries makes it particularly effective in segmenting waterland interfaces and other irregular structures in SAR images. Especially in scenarios with complex target contours (such as the junction of water bodies and land), its segmentation effect is significantly better than that of LSC and the traditional SLIC algorithm. Especially in areas with complex target geometric structures, the EDC-SLIC algorithm shows stronger boundary capture ability and spatial consistency, laying a good foundation for the subsequent extraction of water body information. This comparative analysis clearly underscores the effectiveness of the EDC-SLIC algorithm. By overcoming the limitations of traditional methods in boundary fitting and shape retention, it establishes a more reliable framework for superpixel-based segmentation and offers strong support for remote sensing image interpretation in complex and noise-prone environments.

This comparison result convincingly demonstrates the superiority of EDC-SLIC algorithm based on eight-direction convolution in superpixel segmentation tasks. By effectively addressing the limitations of traditional algorithms—particularly in terms of boundary fitting accuracy and shape preservation—the EDC-SLIC algorithm achieves more refined and coherent segmentation results. Furthermore, its enhanced adaptability to complex textures and noise-prone environments makes it especially suitable for SAR image analysis. This improvement provides a

more robust and reliable technical foundation for high-precision remote sensing interpretation in complex real-world scenarios.

In this article, the accuracy of the superpixel segmentation results is evaluated through three parameters: boundary recall (BR), undersegmentation error (UE), and over-segmentation error (OE). The specific results are shown in Tables I–III.

In the performance evaluation of superpixel segmentation, BR serves as a key metric for assessing the boundary retention capability of segmentation methods. A higher BR value indicates greater accuracy in preserving the true boundaries of objects within the image. Experimental results show that the EDC-SLIC algorithm achieves the highest BR values among the tested methods. This clearly demonstrates that, compared with traditional algorithms such as SLIC and LSC, the EDC-SLIC algorithm offers significant advantages in boundary retention. It can more accurately capture fine details at object edges, performing especially well in complex segmentation tasks where boundary intricacies are prominent.

The UE quantifies the extent to which background regions are mistakenly included within the target area in the segmentation results. A lower UE value indicates better segmentation precision, whereas a higher value suggests that the algorithm fails to effectively separate distinct regions, leading to the unintended merging of areas that should remain distinct. Experimental results show that the UE values of the EDC-SLIC algorithm consistently remain at a relatively low level. This demonstrates that the EDC-SLIC algorithm can significantly minimize undersegmentation errors while preserving regional integrity. By effectively avoiding the erroneous merging of dissimilar regions, the algorithm achieves higher segmentation accuracy and better delineation of object boundaries.

The OE assesses the extent to which the target region is unnecessarily fragmented during the segmentation process. A lower OE value indicates better regional coherence, while a higher value suggests that the segmentation method excessively divides a single homogeneous area into multiple small segments, thereby compromising the integrity of the region. Experimental

Scene	Precision parameter	LSC algorithm	SLIC algorithm	EDC-SLIC algorithm
1	BR	22.75%	16.77%	18.90%
	UE	12.79%	12.58%	12.62%
	OE	21.60%	30.33%	20.85%
	T	2.832	1.886	2.404
2	BR	17.46%	20.15%	20.07%
	UE	9.62%	9.87%	9.15%
	OE	4.60%	6.55%	3.50%
	T	5.611	5.118	7.928
3	BR	17.15%	15.75%	18.20%
	UE	14.72%	8.69%	11.27%
	OE	6.02%	13.43%	6.88%
	T	4.014	2.985	4.260
4	BR	27.91%	28.17%	30.47%
	UE	3.11%	2.74%	3.40%
	OE	10.18%	8.96%	6.71%
	Т	11 716	13.425	13.503

 $\begin{tabular}{l} TABLE III \\ PRECISION RESULTS WHEN THE NUMBER OF SUPERPIXELS IS SET TO 1300 \\ \end{tabular}$ 

Scene	Precision parameter	LSC algorithm	SLIC algorithm	EDC-SLIC algorithm
1	BR	19.49%	12.18%	21.36%
	UE	12.20%	9.10%	10.45%
1	OE	20.87%	36.90%	25.12%
	T	2.531	1.669	2.894
	BR	19.70%	18.13%	24.93%
2	UE	8.16%	10.88%	7.70%
2	OE	3.75%	7.05%	3.23%
	T	7.668	4.238	10.956
	BR	21.00%	16.57%	21.12%
3	UE	12.21%	6.93%	9.94%
3	OE	8.51%	16.45%	7.14%
	T	4.188	3.398	5.083
	BR	27.66%	27.14%	30.15%
4	UE	3.24%	3.54%	3.30%
	OE	7.79%	9.64%	6.81%
	T	12.088	10.482	13.564

comparisons reveal that the EDC-SLIC algorithm outperforms both the traditional SLIC and LSC algorithms in terms of OE. It effectively suppresses over-segmentation, maintaining the continuity and completeness of target regions. This highlights the algorithm's strong suitability for image segmentation tasks that require high preservation of regional structure and integrity.

In summary, the EDC-SLIC algorithm exhibits excellent overall performance. It surpasses traditional algorithms in boundary retention while effectively minimizing both under-segmentation and OEs. These strengths underscore its robust adaptability to complex segmentation scenarios, making it highly valuable for practical applications. Consequently, the EDC-SLIC algorithm offers reliable technical support for achieving high-precision image segmentation tasks.

Furthermore, as evidenced in Figs. 3, 4, and supported by multiple evaluation metrics, the edge segmentation accuracy for water bodies with curved or complex terrain features is observed to improve with an increase in the number of superpixel segments.

# B. Experiment on Extracting Water Body Information

In this article, for the original image data and their corresponding superpixel segmentation results in the same scene, three water body extraction methods are applied: the Niblack local threshold method, the traditional Otsu algorithm, and the MFW-Otsu algorithm. A comparative analysis and accuracy evaluation of these methods are conducted. The specific water body extraction results are illustrated in Fig. 6, where the black regions represent water bodies and the white regions represent the background.

In Fig. 6, panels (a)–(c) respectively show the water body extraction results using the Niblack algorithm without superpixel fusion, the traditional Otsu algorithm, and the MFW-Otsu algorithm across five scenarios. Panels (d)–(f) display the

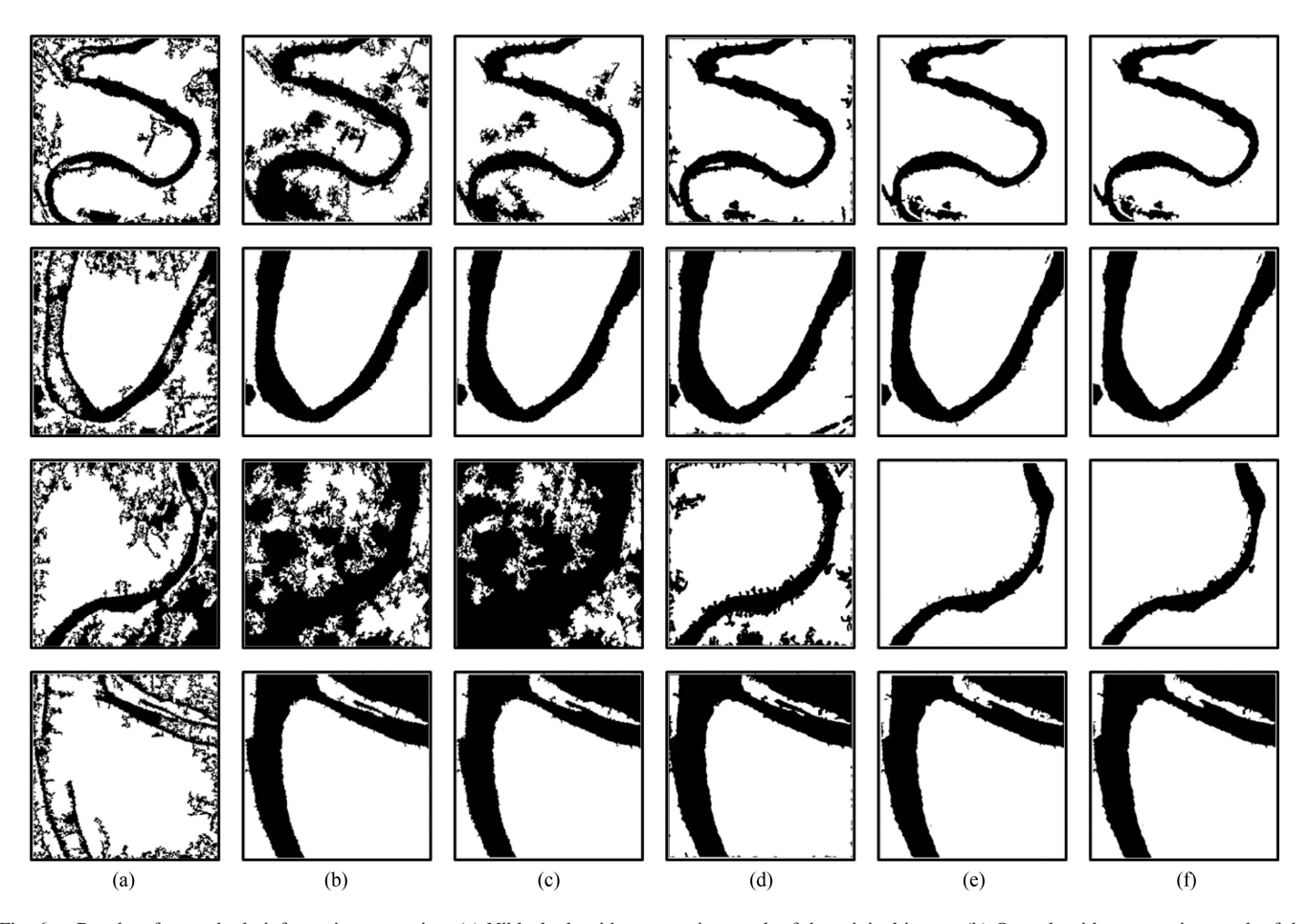


Fig. 6. Results of water body information extraction. (a) Niblack algorithm extraction result of the original image. (b) Otsu algorithm extraction result of the original image. (c) MFW-Otsu algorithm extraction result of the fused superpixels. (e) Otsu algorithm extraction result of the fused superpixels. (f) MFW-Otsu algorithm extraction result of the fused superpixels.

corresponding extraction results of these three algorithms after fusing superpixels. Experimental comparisons indicate that, within the same scene, fusing superpixels leads to significant improvements in boundary integrity, detail preservation, and robustness against noise. In addition, the three algorithms exhibit notable differences in their ability to maintain water boundary integrity, retain fine details, and resist noise interference.

Specifically, the water body extraction results without superpixel fusion—shown in (a)–(c)—generally exhibit more fragmentation and discontinuity. For example, in Scene 1, the extracted water boundaries from all three algorithms appear blurred and suffer from significant noise interference. In terms of detail preservation, these algorithms struggle with complex water boundaries; as seen in Scene 3, many nonwater areas near the water-land junction are incorrectly classified as water. In addition, when confronted with image noise or complex backgrounds, the algorithms without superpixel fusion are more susceptible to interference. Although in Scenes 2 and 4 the unfused extraction results perform relatively well, they still tend to produce noticeable misclassifications in more challenging scenarios.

The water body extraction results fused with superpixels—shown in (d), (e), and (f)—are generally smoother and more

continuous. For instance, in Scene 1, all three algorithms with superpixel integration produce clearer boundaries and improved coherence within the water body regions. Regarding detail preservation, the benefits of superpixel fusion are even more evident. In Scene 3, these algorithms successfully extract fine water body branches and accurately distinguish areas with different depths or color variations, offering more precise data for subsequent water body analysis. Moreover, by considering the overall characteristics of superpixels during fusion, the algorithms demonstrate stronger resistance to noise and interference.

By comparing the water body extraction results of the three algorithms, it is observed that although the Niblack algorithm has certain advantages in handling images with uneven brightness, it is relatively sensitive to noise. This sensitivity leads to significant misclassification in nonwater areas, making accurate water body extraction difficult. In contrast, the traditional Otsu algorithm performs better in delineating water body boundaries and demonstrates a strong noise suppression capability. However, it still faces challenges with complex local backgrounds, often missing small water bodies or producing inaccurate segmentation results.

The MFW-Otsu algorithm demonstrates enhanced robustness and adaptability by effectively integrating both global and

Scene	Precision parameter	Niblack algorithm	Otsu algorithm	MFW-Otsu algorithm
•	OA	0.8505	0.7794	0.8886
1	Kappa coefficient	0.5522	0.4469	0.6508
	F1 score	0.5800	0.5562	0.6999
2	OA	0.8008	0.9848	0.9856
	Kappa coefficient	0.4873	0.9573	0.9592
	F1 score	0.5633	0.9776	0.9792
3	OA	0.7329	0.4977	0.3808
	Kappa coefficient	0.3078	0.1430	0.0867
	F1 score	0.3945	0.2983	0.2499
4	OA	0.7417	0.9805	0.9792
	Kappa coefficient	0.3457	0.9557	0.9528
	F1 score	0.4298	0.9825	0.9815

TABLE IV
EXTRACTION ACCURACY RESULTS OF WATER BODY INFORMATION FROM THE ORIGINAL IMAGE

 $\label{thm:table v} TABLE\ V$  Accuracy Results of Water Body Information Extraction by Integrating Superpixels

Scene	Precision parameter	Niblack algorithm	Otsu algorithm	MFW-Otsu algorithm
	OA	0.9257	0.9538	0.9546
1	Kappa coefficient	0.7469	0.8287	0.8314
	F1 score	0.7725	0.8464	0.8487
	OA	0.9624	0.9837	0.9837
2	Kappa coefficient	0.8988	0.9540	0.9539
	F1 score	0.9379	0.9769	0.9764
	OA	0.8847	0.9861	0.9862
3	Kappa coefficient	0.5914	0.9299	0.9300
	F1 score	0.6569	0.9365	0.9368
	OA	0.9600	0.9729	0.9741
4	Kappa coefficient	0.9111	0.9386	0.9413
	F1 score	0.9574	0.9769	0.9776

local features. It produces smooth and complete water body boundaries, with especially strong segmentation performance in complex background conditions. In addition, this improved algorithm excels at preserving fine details in narrowband regions and significantly outperforms the Niblack and traditional Otsu algorithms in noise suppression and overall extraction accuracy.

In summary, the MFW-Otsu algorithm excels in both extraction accuracy and noise resilience, making it especially well-suited for extracting water body information from SAR images. Its superior performance offers reliable technical support for high-precision water body monitoring and holds promising application potential in the field of remote sensing image processing.

This study systematically compared the three algorithms using three evaluation metrics: OA, Kappa coefficient, and F1 score. The experimental results indicate that the MFW-Otsu algorithm, which integrates weighted mean and local variance, demonstrates significant advantages across all indicators. Furthermore, the incorporation of the superpixel fusion strategy notably enhances the accuracy and adaptability of water body information extraction. The detailed results are presented in Tables IV and V.

In the performance evaluation of water body information extraction, OA serves as a key metric to assess the general classification accuracy of the algorithm—the higher the OA, the

better the overall performance. Experimental results show that the average OA of the MFW-Otsu algorithm with superpixel fusion reaches 0.9747, representing an improvement of 0.06% and 4.45% over the traditional Otsu algorithm (0.9741) and the Niblack algorithm (0.9332), respectively. The Kappa coefficient, which measures the consistency between classification results and ground truth, ranges from -1 to 1, with higher values indicating stronger agreement. The average Kappa coefficient of the MFW-Otsu algorithm after superpixel fusion is 0.9142, exceeding the traditional Otsu algorithm (0.9128) by 0.15% and the Niblack algorithm (0.7871) by 16.15%. The F1 score, the harmonic mean of precision and recall, comprehensively reflects the balance between classification accuracy and completeness, especially valuable in imbalanced class scenarios. For the MFW-Otsu algorithm with superpixel fusion, the average F1 score reaches 0.9349, which is 0.07% and 12.47% higher than those of the traditional Otsu algorithm (0.9342) and the Niblack algorithm (0.8312), respectively.

Furthermore, the accuracy results demonstrate that integrating superpixel fusion significantly enhances the robustness and detail-processing capability of the algorithm in complex scenes. It enables the precise extraction of fine water body features such as tiny branches and areas with varying depths. For example, in Scene 3, the OA of the traditional Otsu algorithm on the original image is 0.4977. After superpixel fusion, the OA rises sharply to

0.9861, an increase of 0.4884. Similarly, the Kappa coefficient improves from 0.1430 to 0.9299, increasing by 0.7869. The F1 score also shows a notable increase from 0.2983 to 0.9365, a gain of 0.6382. These results clearly indicate that superpixel fusion greatly boosts the adaptability of the Otsu algorithm to complex scenes, effectively reducing misclassification and achieving more accurate water body extraction.

Based on the above-mentioned experimental results, the MFW-Otsu algorithm demonstrates strong performance across key metrics such as classification accuracy, consistency, and precision. Compared with the Niblack algorithm and the traditional Otsu algorithm, the MFW-Otsu algorithm not only significantly improves classification accuracy but also enhances adaptability to local feature variations, exhibiting greater robustness in handling complex backgrounds. Moreover, the integration of the superpixel fusion strategy further boosts the accuracy and adaptability of water body extraction, significantly enhancing the algorithm's capability to process fine details, especially in challenging scenarios. These strengths enable the MFW-Otsu algorithm to more effectively distinguish water body regions within complex backgrounds. By improving classification accuracy, consistency, and stability, this approach holds broad potential for practical applications and wide promotion in remote sensing image analysis.

#### V. CONCLUSION

This study proposes a refined water extraction method for SAR images based on superpixel segmentation. By integrating the EDC-SLIC superpixel segmentation algorithm with the MFW-Otsu algorithm, the method significantly enhances the accuracy and robustness of water extraction. Experimental results demonstrate that the EDC-SLIC algorithm outperforms traditional LSC and SLIC algorithms in key metrics such as boundary retention, UE, and OE, exhibiting superior adaptability and stability in complex scenarios. Meanwhile, the MFW-Otsu algorithm effectively boosts water body extraction accuracy by combining global and local features, showing excellent performance in complex backgrounds and noise conditions.

In superpixel segmentation, the EDC-SLIC algorithm enhances edge sensitivity and texture capture by incorporating eight-direction convolution features, allowing superpixel boundaries to more accurately conform to the complex contours of targets. For water body extraction, the MFW-Otsu algorithm improves adaptability to local feature variations, effectively reduces noise interference, and boosts the accuracy of water body recognition by weighting local mean and variance.

Overall, the method proposed in this article demonstrates strong performance across multiple evaluation metrics. It not only improves the accuracy and consistency of water body extraction but also significantly enhances adaptability to complex scenarios. This approach offers a novel and effective technical solution for extracting water body information from SAR images, with broad application prospects. It holds important practical significance in areas such as water resource management, environmental monitoring, and disaster early warning.

It should be noted that the proposed MFW-Otsu method incorporates superpixel segmentation as a preprocessing step, which enhances extraction accuracy but increases algorithmic complexity, leading to lower computational efficiency compared with traditional Niblack and Otsu algorithms. Future work will focus on improving efficiency, integrating multisource data and deep learning to strengthen automation and generalization, and extending validation to complex large-scale scenarios with critical comparisons against SAR-specific superpixel approaches such as Gamma-SLIC and PolSAR-SLIC.

#### REFERENCES

- Y. Cunjian, W. Yiming, W. Siyuan, Z. Zengxiang, and H. Shifeng, "Extracting the flood extent from satellite SAR image with the support of topographic data," in *Proc. Int. Conf. Info-Tech Info-Net*, 2001, pp. 87–92.
- [2] J. Tan et al., "A self-adaptive thresholding approach for automatic water extraction using sentinel-1 SAR imagery based on OTSU algorithm and distance block," *Remote Sens.*, vol. 15, no. 10, 2023, Art. no. 2690.
- [3] C. Cazals et al., "Mapping and characterization of hydrological dynamics in a coastal marsh using high temporal resolution sentinel-1A images," *Remote Sens.*, vol. 8, no. 7, 2016, Art. no. 570.
- [4] Y. Tian, X. Chen, P. Luo, and Y. Xu, "Beijiang water body information extraction based on ENVISAT-ASAR," in *Proc. IEEE 2nd Int. Workshop Earth Observ. Remote Sens. Appl.*, 2012, pp. 273–277.
- [5] S. Hong et al., "Water area extraction using RADARSAT SAR imagery combined with landsat imagery and terrain information," *Sensors*, vol. 15, no. 3, pp. 6652–6667, 2015.
- [6] B. Linan, L. Xiaolei, and Y. Jingchuan, "Water extraction in SAR images using features analysis and dual-threshold graph cut model," *Remote Sens.*, vol. 13, no. 17, pp. 3465–3465, 2021.
- [7] C. Y. Soo, "Water body extraction in SAR image using water body texture index," *Korean J. Remote Sens.*, vol. 31, no. 4, pp. 337–346, 2015.
- [8] J. Liang and D. Liu, "A local thresholding approach to flood water delineation using Sentinel-1 SAR imagery," ISPRS J. Photogrammetry Remote Sens., vol. 159, pp. 53–62, 2020.
- [9] Y. Shao, S. Wang, W. Tian, H. Gong, and F. Zhang, "Fast extracting and change detection of dammed lakes using highresolution SAR images: A case study of Tangjiashan Dammed Lake," in *Proc. IEEE Int. Geosci. Remote Sens. Symp.*, 2009, pp. II–349–II–352.
- [10] Y. Leng and N. Li, "Improved change detection method for flood monitoring," *J. Radars*, vol. 6, pp. 204–212, 2017.
- [11] S. Cao, Z. Ye, D. Xu, and X. Xu, "A hadamard product based method for DOA estimation and gain-phase error calibration," *IEEE Trans. Aerosp. Electron. Syst.*, vol. 49, no. 2, pp. 1224–1233, Apr. 2013.
- [12] L. Ying et al., "Improved ACM algorithm for Poyang lake monitoring," J. Electron. Inf. Technol., vol. 39, no. 5, pp. 1064–1070, 2017.
- [13] Z. Wenbin et al., "Water extraction method based on multi-texture feature fusion of synthetic aperture radar images," *Sensors*, vol. 21, no. 14, pp. 4945–4945, 2021.
- [14] P. Zhang et al., "Automatic extraction of water and shadow from SAR images based on a multi-resolution dense encoder and decoder network," *Sensors*, vol. 19, no. 16, pp. 3576–3576, 2019.
- [15] C. Lifu et al., "Towards transparent deep learning for surface water detection from SAR imagery," *Int. J. Appl. Earth Observ. Geoinf.*, vol. 118, 2023, Art. no. 103287.
- [16] G. Reham, "Deep learning for automatic extraction of water bodies using satellite imagery," *J. Indian Soc. Remote Sens.*, vol. 51, no. 7, pp. 1511–1521, 2023.
- [17] L. Junjie et al., "Accurate water extraction using remote sensing imagery based on normalized difference water index and unsupervised deep learning," J. Hydrol., vol. 612, 2022, Art. no. 128202.
- [18] B. Zhao et al., "Deep learning approach for flood detection using SAR image: A case study in Xinxiang," *Int. Arch. Photogrammetry Remote Sens. Spatial Inf. Sci.*, vol. 43, pp. 1197–1202, 2022.
- [19] X. Chuan et al., "SAR image water extraction using the attention U-net and multi-scale level set method: Flood monitoring in South China in 2020 as a test case," *Geo-Spatial Inf. Sci.*, vol. 25, no. 2, pp. 155–168, 2022.
- [20] X. Dazhi et al., "Difference-guided multiscale graph convolution network for unsupervised change detection in PolSAR images," *Neurocomputing*, vol. 555, 2023, Art. no. 126611.

- [21] F. Zhang et al., "Superpixelwise likelihood ratio test statistic for PolSAR data and its application to built-up area extraction," *ISPRS J. Photogram-metry Remote Sens.*, vol. 209, pp. 233–248, 2024.
- [22] D. Xiang, X. Pan, H. Ding, J. Cheng, and X. Sun, "Two-stage registration of SAR images with large distortion based on superpixel segmentation," *IEEE Trans. Geosci. Remote Sens.*, vol. 62, 2024, Art. no. 5211115, doi: 10.1109/TGRS.2024.3392971.
- [23] J. Feng, Z. Cao, and Y. Pi, "Polarimetric contextual classification of PolSAR images using sparse representation and superpixels," *Remote Sens.*, vol. 6, no. 8, pp. 7158–7181, 2014.
- [24] H. Gao, C. Wang, D. Xiang, J. Ye, and G. Wang, "TSPol-ASLIC: Adaptive superpixel generation with local iterative clustering for time-series quadand dual-polarization SAR data," *IEEE Trans. Geosci. Remote Sens.*, vol. 60, 2022, Art. no. 5217015, doi: 10.1109/TGRS.2021.3126669.
- [25] Y. Chen et al., "Extraction of urban water bodies from high-resolution remote-sensing imagery using deep learning," *Water*, vol. 10, no. 5, pp. 585–585, 2018.
- [26] O. A. Pappas, N. Anantrasirichai, A. M. Achim, and B. A. Adams, "River planform extraction from high-resolution SAR images via generalized gamma distribution superpixel classification," *IEEE Trans. Geosci. Re*mote Sens., vol. 59, no. 5, pp. 3942–3955, May 2021.
- [27] C. Xiaopeng et al., "All-weather and superpixel water extraction methods based on multisource remote sensing data fusion," *Remote Sens.*, vol. 14, no. 23, pp. 6177–6177, 2022.
- [28] W. Haoming et al., "Water extraction in PolSAR image based on superpixel and graph convolutional network," *Appl. Sci.*, vol. 13, no. 4, pp. 2610–2610, 2023.
- [29] T. Zhao et al., "SPT-UNet: A superpixel-level feature fusion network for water extraction from SAR imagery," *Remote Sens.*, vol. 16, no. 14, pp. 2636–2636, 2024.
- [30] N. Li et al., "Multiscale adaptive PolSAR image superpixel generation based on local iterative clustering and polarimetric scattering features," *ISPRS J. Photogrammetry Remote Sens.*, vol. 220, pp. 307–322, 2025.
- [31] Z. Li and J. Chen, "Superpixel segmentation using Linear Spectral Clustering," in *Proc. IEEE Conf. Comput. Vis. Pattern Recognit.*, pp. 1356–1363, 2015.
- [32] R. Achanta et al., "SLIC superpixels," 2010.
- [33] N. Otsu, "A threshold selection method from gray-level histograms," *IEEE Trans. Syst., Man, Cybern.*, vol. 9, no. 1, pp. 62–66, Jan. 1979.



**Xiaoxiao Ma** was born in 2000. She received the B.E. degree in remote sensing science and technology from Henan Polytechnic University in Jiaozuo, China, in 2022, and the M.S. degree in electronic information with Jiangsu Normal University, Xuzhou, China, in 2025

She majors in water body extraction from synthetic aperture radar images.



Ning Sun was born in 1998. He received the B.E. degree in surveying and mapping engineering from the College of Civil Engineering, Nanjing Forestry University, Nanjing, China, in 2021, and the M.S degree in electronic information with Jiangsu Normal University, Xuzhou, China, in 2025.

He majors in synthetic aperture radar image processing.



Lianpeng Zhang received the M.S. degree in geodesy and survey engineering from the Shandong University of Science and Technology, Taian, China, in 1989, and the Ph.D. degree in photogrammetry and remote sensing from the Shandong University of Science and Technology, Qingdao, China, in 2003

He is currently a Professor with the School of Geography, Geomatics and Planning, Jiangsu Normal University, Xuzhou, China. His research interests include high-resolution image processing and computer vision in urban remote sensing applications.



**Fengcheng Guo** was born in 1992. He received the Ph.D. degree in photogrammetry and remote sensing from the State Key Laboratory of Information Engineering in Surveying Mapping, and Remote Sensing (LIESMRS), Wuhan University, Wuhan, China, in 2020

Since 2020, he has been with the School of Geography, Geomatics and Planning, Jiangsu Normal University, where he became an Associate Professor in 2022. He majors in SAR image processing.



Wensong Liu received the M.S. degree in surveying and mapping from China University of Petroleum, Qingdao, China, in 2016, and the Ph.D. degree in photogrammetry and remote sensing from Wuhan University, Wuhan, China, in 2019

He is currently an Associate Professor and Researcher with School of Geography, Geomatics and Planning, Jiangsu Normal University, Xuzhou, China. His research interests include PolSAR images processing and change detection.